Applied Catalysis B: Environmental 254 (2019) 479–490

Contents lists available at ScienceDirect

Applied Catalysis B: Environmental

journal homepage: www.elsevier.com/locate/apcatb

Mediator-free direct dual-Z-scheme $Bi_2S_3/BiVO_4/MgIn_2S_4$ composite photocatalysts with enhanced visible-light-driven performance towards carbamazepine degradation

Yan Guo, Yanhui Ao*, Peifang Wang*, Chao Wang

Key Laboratory of Integrated Regulation and Resource Development on Shallow Lakes, Ministry of Education, College of Environment, Hohai University, No.1, Xikang road, Nanjing, 210098, China

ARTICLE INFO

Keywords:
Dual Z-scheme
Bi_2S_3
$BiVO_4$
$MgIn_2S_4$
Carbamazepine

ABSTRACT

The development of visible-light-driven photocatalysts with high photocatalytic performance is a desired research direction of scholars for energy crisis mitigation and environment restoration. In this study, a series of highly active mediator-free direct dual-*Z*-scheme $Bi_2S_3/BiVO_4/MgIn_2S_4$ hybrid photocatalysts were controllably synthesized by a in-situ growth method for the first time. XRD manifested the coexistence of $MgIn_2S_4$, $BiVO_4$ and Bi_2S_3 in the as-prepared nanocomposites. The intimate 2D-2D hetero-junction interfaces between $BiVO_4$ and $MgIn_2S_4$ as well as $BiVO_4$ and Bi_2S_3 in the hybrid photocatalysts were verified by TEM and HRTEM. The photocatalytic performance of as-fabricated catalysts was estimated by the degradation of carbamazepine (CBZ) under visible light illumination. The results demonstrated that the as-constructed $Bi_2S_3/BiVO_4/MgIn_2S_4$ composites displayed significantly improved photocatalytic activity for CBZ degradation by factors of 44.9 and 423.1 compared to $MgIn_2S_4$ and $BiVO_4$, respectively. The enhanced photocatalytic performance of $Bi_2S_3/BiVO_4/MgIn_2S_4$ composites was actually ascribed to the direct dual-*Z*-scheme migration mechanism, which was proved by XPS analysis, trapping experiments and ESR results. The formation of direct dual-*Z*-scheme efficiently enhanced the separation of charge carriers. Furthermore, according to DRS, the expanded light absorption in visible wavelength region also contributed to the boosted photocatalytic activity of $Bi_2S_3/BiVO_4/MgIn_2S_4$ composites. The photocatalytic degradation products of CBZ were detected and a tentative degradation pathway was proposed.

1. Introduction

Carbamazepine (CBZ), an antiepileptic pharmaceutical, is used extensively to treat epilepsy and depressive disorder [1]. Because of its nature of symmetrical aromatic heterocyclic structure, carbamazepine is hard to be biodegraded and has the characteristics of bioaccumulation and persistence [2]. Attentively, CBZ has been continually detected in aquatic environment including surface water, underground water and even drinking water, which would induce to potentially serious threat to ecosystem [3–5]. Therefore, an efficient approach is urgently needed for elimination of CBZ from watery environment. In the past few years, advanced oxidation processes (AOPs), including photocatalytic technology, have been demonstrated to be preponderant technologies for the mineralization of pharmaceuticals and other organic micro-pollutants in tertiary municipal sewage treatment. Thereinto, photocatalysis has been widely investigated for the abatement of various recalcitrant pharmaceutical drug because of its well-known superiority [6–9]. To date, numerous composite materials have been developed and have been used to degrade organic pollutants because of their advantages over their corresponding single components.

For various developed and applied composite materials, the investigations of new functional materials are fairly active in international research, such as delafossite [10,11], scheelite [12,13], perovskite [14–17] and spinel-type materials [18,19]. Among them, Spinel-type materials is a kind of photocatalyst with good development potentiality and application foreground because of the existence of cationic holes and high-surface-energy quarter spherical defect in its structure [20]. The ternary metal indium sulfides with spinel structure (AIn_2S_4, A = Zn, Cd, Ca, Mg) have aroused worldwide concern because of their optoelectronic property, chemical stability, unique electronic structure, especially excellent photocatalytic performance [21–23]. The above advantages provided AIn_2S_4 widespread photocatalytic

* Corresponding authors.
E-mail addresses: andyao@hhu.edu.cn (Y. Ao), pfwang2005@hhu.edu.cn (P. Wang).

https://doi.org/10.1016/j.apcatb.2019.04.031
Received 22 February 2019; Received in revised form 5 April 2019; Accepted 11 April 2019
Available online 27 April 2019
0926-3373/

applications in pollutant degradation [24,25], water splitting [26,27], CO_2 reduction [28,29] and bacterial inactivation [30,31]. In particular, $MgIn_2S_4$ as one of AIn_2S_4 materials has been known long before and gained plenty of researches [32,33]. $MgIn_2S_4$ is a typical visible-light-driven photocatalyst with a desirable direct band gap of 2.1–2.28 eV [32]. However, $MgIn_2S_4$ has rarely been investigated in photocatalysis field by far. Liu's group successfully prepared g-C_3N_4/$MgIn_2S_4$ composites with conventional heterojunction structure which displayed enhanced photocatalytic performance in reducing 4-nitroaniline and degrading methyl orange [34]. Although the separation efficiency of charge carriers was enhanced via coupling g-C_3N_4 with $MgIn_2S_4$, reduction/oxidation activity of the photoinduced electrons/holes was decreased because of the transferring between two semiconductors. Instead of traditional heterostructure, Z-scheme photocatalytic pattern with unique charge migration mechanism have been developed to take efficient charge separation and strong redox ability into account simultaneously [35–37]. Therefore, semiconductor with a more positive valence band edge should be considered into the synthesis of Z-scheme-type $MgIn_2S_4$-based photocatalysts. In this way, photo-excited electrons in CB of $MgIn_2S_4$ and holes in VB of selected semiconductor with higher potential could be effectively separated and then participate in photocatalytic redox reaction synchronously.

Alternatively, Bismuth Vanadate ($BiVO_4$) as typical visible-light-active Bi-system semiconductors are commonly investigated by researchers recently. The advantages of narrow energy gap (Eg ˜ 2.4–2.5 eV), adjustable electronic structure, easy synthesis and high stability amplified its application in the field of photocatalysis [38,39]. In despite of the lower conduction band position, $BiVO_4$ possess fairly adequate valence band potential for the generation of holes and reactive oxygen species with strong oxidation ability [36]. Hence, $BiVO_4$ is suitable for the preparation of Z-scheme-type composite photocatalysts. Already, $BiVO_4$ have been employed to assemble Z-scheme-type hybrid photocatalysts coupling with other catalysts. Such as $BiVO_4$/Au@CdS [37] and $BiVO_4$/Ag/Cu_2O [38] for pollution removal, $BiVO_4$/CDs/CdS [39] and Co_3O_4/$BiVO_4$ [40] for H_2 generation, RGO-CoO_x/$BiVO_4$ [41] for CO_2 reduction, AgI/$BiVO_4$ [42] for bacteria disinfection. The results indicated that all of these composites exhibited considerable enhancement on their photocatalytic performance compared with pure semiconductors, which were attributed to Z-scheme migration pattern.

On the other hand, Bi_2S_3, as another Bi-based semiconductor, has attracted much attention owing to its narrow band-gap, large absorption coefficient and so on [43,44]. Bi_2S_3 also has been chosen to design Z-scheme composites because of its higher conduct band potential and lower valence band potential [45]. According to previous literature, Bi_2S_3 was easily generated and attached to the surface of $BiVO_4$ to form $BiVO_4$/Bi_2S_3 composites in the presence of sulfur source ascribing to the strong interaction between Bi^{3+} and S^{2-} ions after the secondary hydrothermal process of pure $BiVO_4$ [46–48]. Moreover, Wang et al. [49] successfully synthesized tri-component $BiVO_4$/Bi_2S_3/MoS_2 heterojunction through a facile in-situ hydrothermal method. At the same time, the intermediate Bi_2S_3 was easily formed on the surface of $BiVO_4$ during the MoS_2 was coupled on the $BiVO_4$ with thioacetamide as sulfur source.

In light of the above view, we made an attempt to design a direct dual-*Z*-scheme-type heterostructured Bi_2S_3/$BiVO_4$/$MgIn_2S_4$ hybrid photocatalysts via an in-situ growth hydrothermal method. In the preparation process, both $MgIn_2S_4$ and Bi_2S_3 grew simultaneously on the surface of $BiVO_4$. The photocatalytic activities of the as-fabricated nanocomposites were evaluated by degradation of CBZ under visible light illumination. The mechanism of performance improvement based on direct dual-*Z*-scheme migration pattern rather than the conventional heterojunction type was elaborated. Subsequently, we also put forward the possible degradation pathways of CBZ based on the intermediates identified by HPLC-MS technology.

2. Experimental section

The methyl alcohol, acetonitrile and formic acid used in high performance liquid chromatography (HPLC) and liquid chromatography tandem mass spectrometry (LC-ESI-MS/MS) system were of spectrum pure. Other chemicals were purchased with analytical grade and used directly without further purification. Ultrapure water were used to prepare all solution during whole experimental process.

2.1. Synthesis of $BiVO_4$

Under vigorous stirring condition, 0.97 g $Bi(NO_3)_5$·$5H_2O$, 0.05 g CTAB (hexadecyl trimethyl ammonium bromide) and 0.8 g Na_3VO_4·$12H_2O$ were added into 80 mL water in sequence with a time interval of 10 min. After 30 min stirring, the mixed suspension was dumped into 100 mL Teflon-lined stainless steel autoclave and treated at 120 ∘C for 24 h. Prior to drying at 60 ∘C for subsequent use, the white precipitate was obtained after centrifugation and washed by plenty of water.

2.2. Synthesis of Bi_2S_3/$BiVO_4$/$MgIn_2S_4$ composites

Firstly, 1 mmol $Mg(NO_3)_2$·$6H_2O$ and 2 mmol $In(NO_3)_3$·$4.5H_2O$ were thoroughly dissolved in 70 mL water. Subsequently, a certain amount of as-prepared $BiVO_4$ was dispersed in the solution and treated with ultrasonic for 1 h, followed by adding 8 mmol TAA (thioacetamide) under stirring. The suspension was poured into 100 mL Teflon-lined stainless steel autoclave and maintained at 180 ∘C for 12 h. After cooling down to ambient temperature, the product was centrifuged and washed with a large amount of ethanol and water. Finally, the sample was dried at 60 ∘C. The Bi_2S_3/$BiVO_4$/$MgIn_2S_4$ composites with different mass ratios were synthesized by altering the adding quantity of $BiVO_4$. The synthesized Bi_2S_3/$BiVO_4$/$MgIn_2S_4$ composites were marked as BS/BVO/MIS-*x* (x = 1, 2.5, 5, 15, 25, 40 and 60), which corresponded to the mass ratios of $BiVO_4$ to $MgIn_2S_4$ with 1%, 2.5%, 5%, 15%, 25%, 40% and 60%, respectively. Bare $MgIn_2S_4$ was prepared according to the same process without the addition of $BiVO_4$.

2.3. Characterization

The crystal phase structure and composition of the as-obtained photocatalysts were identified by the powder X-ray diffraction (XRD, Rigaku, SmartLab) with scan range from 10°–70°. Transmission electron microscopy (TEM) and high resolution transmission electron microscopy (HRTEM) were implement on a JEM-2100 apparatus. A UV–vis spectrophotometer (Shimadzu, UV3600) was employed to record the UV–vis diffuse reflectance spectra (DRS) of the as-obtained catalysts. The BET surface areas were obtained via the nitrogen adsorption–desorption isotherms using a Micromeritics ASAP 2000 apparatus. The X-ray photoelectron spectroscopy (XPS) was obtained from a Thermo X-ray photoelectron spectrometer. Photoluminescence (PL) spectra were measured on a Hitachi fluorescence spectrophotometer. The active species during the photocatalytic reaction were detected by trapping experiment and electron spinresonance spectroscopy (ESR, JES FA200).

2.4. Photocatalytic experiment

The photocatalytic performance of as-synthesized catalysts were evaluated by the decomposition of carbamazepine under visible light illumination of a 300 W xenon lamp (Zhong jiaojinyuan, CEL-HXF300) with a 400 nm cut-off optical filter. Typically, 50 mg as-synthesized sample was dispersed in 100 mL CBZ solution with initial concentration of 5 mg/mL by ultrasonic processing for 2 min. Before the light irradiation, the suspension was stirred for 60 min in dark to establish the adsorption-desorption equilibrium. 1.5 mL of liquid was sampled at a

prescribed interval and filtrated through a 0.22 μm membrane for purification. The high performance liquid chromatography (HPLC) was used to analyze the above-mentioned filtrate containing CBZ quantitatively.

2.5. Chemical analysis

The concentration of CBZ collected during photocatalytic reaction was measured by HPLC equipped with a Waters e2695 Series system, using a UV detector at an excited wavelength of 210 nm. 20 μL of filtrate injected was eluted by mobile phase consisting of methyl alcohol and ultrapure water (60/40, v/v) with a flow rate of 1.0 mL/min. The column temperature was set at 25 ∘C. LC-ESI-MS/MS system (Agilent 1290/6460 Triple Quad LC/MS) was employed to detect the degradation intermediates for exploring the degradation pathway of CBZ. Under electrospray positive ion (ESI^+) mode, the gradient elution process was performed in chromatographic separation with acetonitrile (solvent A) and ultrapure water containing 0.1%v formic acid (solvent B) as mobile phase. The basic flow of the elution operation was as follows. 10% B was set as the initial eluent condition and kept for 5 min, gradually increasing to 70% in 25 min holding for 10 min, and the mobile phase was finally returned to initial condition in 10 min. In full scan mode, the system was operated for 50 min with the flow rate of 0.24 mL/min to identify degradation products of CBZ.

3. Results and discussion

3.1. Catalyst characterization

The typical powder XRD patterns for the $MgIn_2S_4$, $BiVO_4$ and BS/BVO/MIS composites with different amounts of $BiVO_4$ were displayed in Fig. 1. The diffraction peaks of the obtained pristine $MgIn_2S_4$ and $BiVO_4$ were separately assigned to cubic structure (JCPDS card no.31-0792) [33] and monoclinic phase (JCPDS card no.14-0688) [50]. Concretely, the distinct peaks of $MgIn_2S_4$ could be observed at 2θ values of 23.5°, 27.6°, 33.4°, 43.9°, 48.0°, 56.3° and 59.8° matching with (220), (311), (400), (511), (440), (533) and (444), respectively. And more notably, the patterns of BS/BVO/MIS composites could be indexed to both characteristic diffraction peaks of cubic $MgIn_2S_4$ and monoclinic $BiVO_4$ demonstrating that $MgIn_2S_4$ and $BiVO_4$ were successfully assembled in one composite. With the content of $BiVO_4$ increased from 1% to 60%, the dominance of $MgIn_2S_4$ was declined while $BiVO_4$ was advanced. Additional peaks were also detected at 17.6°, 22.4°, 23.7°, 25.0°, 31.8°, 35.6° and 52.7°, corresponding to the characteristic reflections of the (120), (220), (101), (130), (221), (240) and (312) crystal planes of Bi_2S_3 (JCPDS card no.17-0320) [46,51] generated in the synthesis process of BS/BVO/MIS composites. The intense and sharp diffraction peaks manifested that the prepared photocatalysts were well crystallized [52].

The morphologies and microstructures of the catalysts were ascertained by TEM and HRTEM, and the obtained results are displayed in Fig. 2. $MgIn_2S_4$ with nanosheet-shaped structure were observed from TEM image (Fig. 2A). As shown in Fig. 2B, $BiVO_4$ revealed rod-like structures with 2D morphology. For BS/BVO/MIS-25 composites, it can be seen in Fig. 2C that $MgIn_2S_4$ nanosheets and $BiVO_4$ nanorods were co-existed. It was obvious that sheet-like $MgIn_2S_4$ were immobilized on the surface of $BiVO_4$ nanorods to form intimate contacts, which could be testified by HRTEM in depth. As can be seen from HRTEM image of BS/BVO/MIS-25 (Fig. 2D), the crystal lattice with lattice distances of 0.323 nm was assigned to the (311) facet of $MgIn_2S_4$ (JCPDS card no.31-0792). While interplanar spacing of 0.255 and 0.504 nm, separately corresponding to the (002) plane of $BiVO_4$ (JCPDS card no.14-0688) and (120) plane of Bi_2S_3 (JCPDS card no.17-0320), were detected concurrently. Thus it can be seen that $MgIn_2S_4$, $BiVO_4$ and Bi_2S_3 were co-existed in BS/BVO/MIS composite. And among them, Bi_2S_3 were generated and attached to the surface of $BiVO_4$. Between $MgIn_2S_4$ and $BiVO_4$, a boundary considered as the 2D-2D hetero-junction interface was visually observed in Fig. 2D, which was supposed to boost photo-induced charge separation [53,54]. In view of the TEM and HRTEM results, the hetero-junctions between $MgIn_2S_4$ and $BiVO_4$, $BiVO_4$ and Bi_2S_3 were formed during the hydrothermal synthesis of $Bi_2S_3/BiVO_4/MgIn_2S_4$ composites, which was consistent with anterior XRD results.

The surface chemical compositional identification and electronic state analysis of as-synthesized catalysts were investigated by the XPS spectra which are shown in Fig. 3. As illustrated in the survey spectra (Fig. 3A), Bi, V and O elements were observed in the surface of $BiVO_4$ while Mg, In and S element in $MgIn_2S_4$. With regard to BS/BVO/MIS-25 composite, all elements of $MgIn_2S_4$ and $BiVO_4$ were detected in BS/BVO/MIS-25 hybrid. Consistent with the XRD results, the full-range XPS spectra further corroborated that BS/BVO/MIS-25 was composed

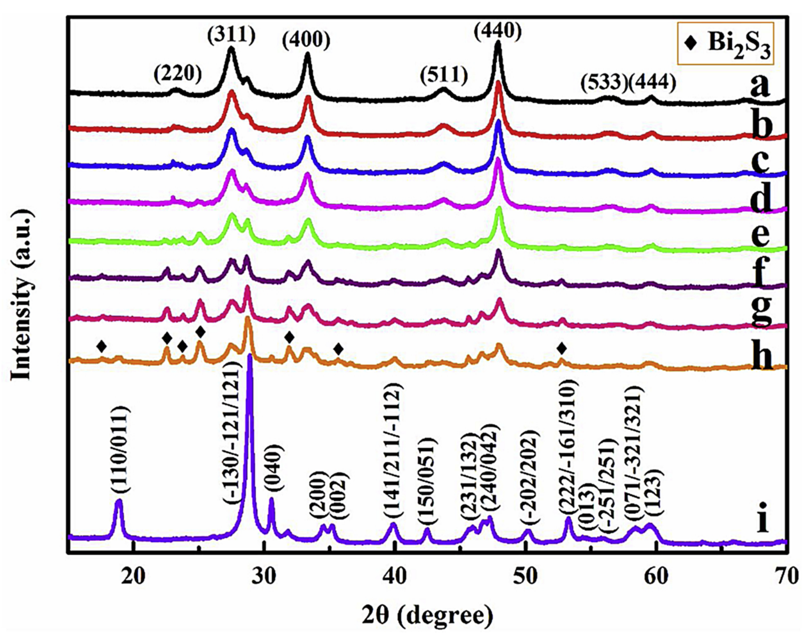

Fig. 1. Typical XRD patterns of $MgIn_2S_4$ (a), BS/BVO/MIS-x (x = 1 (b), 2.5 (c), 5 (d), 15 (e), 25 (f), 40 (g) and 60 (h)) and $BiVO_4$ (i).

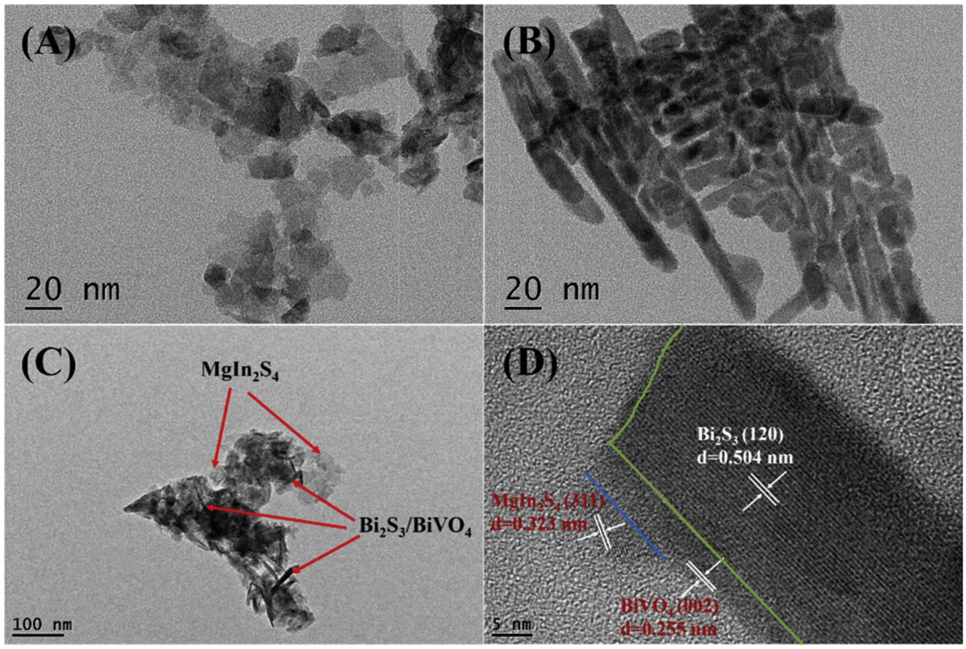

Fig. 2. TEM images of (A) $MgIn_2S_4$ nanosheets, (B) $BiVO_4$ nanorods and (C) BS/BVO/MIS-25; and HRTEM image of (D) BS/BVO/MIS-25 composites.

of $MgIn_2S_4$ and $BiVO_4$ simultaneously. Reference carbon C 1 s at 284.8 eV was employed to rectify binding energy analyses [33,55]. In terms of high-resolution XPS spectra in Fig. 3(B–F), only a single peak at 1305.6 eV was identified as the characteristic peak of Mg 1 s in $MgIn_2S_4$, representing to the Mg^{2+} [56]. The two symmetric peaks at 452.9 eV and 445.3 eV were assigned to In $3d_{3/2}$ and In $3d_{5/2}$ of $MgIn_2S_4$, respectively [57]. According to peak-differentation-imitating analysis, two splitting peaks with binding energies of 163.3 eV and 162.0 eV were severally in accordance with S $2p_{1/2}$ and S $2p_{3/2}$ of S^{2-} [33]. The Bi $4f_{5/2}$ and Bi $4f_{7/2}$ were recorded at about 163.7 and 158.4 eV, respectively [58,59]. The bind energies of V $2p_{1/2}$ and V $2p_{3/2}$ centered at 523.9 and 516.2 eV were associated with pentavalent vanadium of $BiVO_4$ [60]. For the O spectra, the O 1 s was split to O—H bond (531.8 eV), V—O (530.5 eV) and Bi-O bond (529.3 eV) [61]. Interestingly and prominently, the binding energies of Mg 1 s, In 3d and S 2p in BS/BVO/MIS-25 were slightly lower than that of pristine $MgIn_2S_4$. While the binding energies of Bi 4f, V 2p and O 1 s were higher than that of pure $BiVO_4$. Such migration shifts in the binding energies may be attributed to the changed electronic density on the surfaces of assembled $MgIn_2S_4$, $BiVO_4$ and Bi_2S_3 coexisting simultaneously in BS/BVO-MIS-25 [62], suggesting that the interface were generated between them by the interior interaction [63]. To the best of our knowledge, the shift in the binding energy was corresponded to the change in electron density, in which positive shifts represents decreased electron densities but negative shifts for increased electron densities [62]. Therefore, we deduced that the migration direction of photo-induced electrons were from the surface of $BiVO_4$ to that of $MgIn_2S_4$ and Bi_2S_3 in the $Bi_2S_3/BiVO_4/MgIn_2S_4$ composites [64], which was favorable to separate electron-hole pairs and consequently improved photocatalytic performance.

The UV–vis DRS was applied to assess the optical absorption properties of the as-fabricated samples in different wavelength region, which was exhibited in Fig. 4. As can be seen from Fig. 4A, the absorption edges of $MgIn_2S_4$ and $BiVO_4$ were determined at 620 nm [33] and 515 nm [55] respectively, which was the evidence of high visible light response for this two pure samples. Remarkably, a gradually red shift was produced in optical absorption of BS/BVO/MIS composites after assembling $MgIn_2S_4$ and $BiVO_4$, which was in favor of photocatalytic degradation reaction. With regard to BS/BVO/MIS composites, the optical absorption intensities in visible wavelength region were strengthened beyond that of $MgIn_2S_4$ in pace with the amount of the introduced $BiVO_4$ increased. The reasons may go as follows. On the one hand, as for composites, the contact barrier was lowered whereas electronic coupling was reinforced as soon as the heterojunction (intense joint) formed between $MgIn_2S_4$ and $BiVO_4$ [33,65]. In addition, according to the literature, Bi_2S_3 has strong absorption in nearly all of the visible light range because of its small band gap and large absorption coefficient [48]. Therefore, the boosted intensities in visible wavelength region could be ascribed to the generated Bi_2S_3 during the synthesis of BS/BVO/MIS composites, which were dovetailed with XRD results. As a result, the visible light absorptions of coupled composites were reinforced and the corresponding photocatalytic activities were improved consequently. The band gap energies (E_g) of $MgIn_2S_4$ and $BiVO_4$ were respectively ascertained to be 2.18 eV and 2.52 eV from the plots of $(ah\nu)^2$ versus the photon energy ($h\nu$) (Fig. 4B). It's important to note that $MgIn_2S_4$ and $BiVO_4$ all were direct optical transition pattern [66,67].

The nitrogen adsorption-desorption isotherms were measured to investigate the textural properties of as-obtained $MgIn_2S_4$, BS/BVO/MIS composites and $BiVO_4$ samples. As exhibited in Fig. S1 in the Supporting Information, all the isotherms were recognized as type-IV isotherms with type H3 hysteresis loops according to the Brunauer-Deming-Deming-Teller (BDDT) classification, testifying that all the catalysts present mesoporous structure (2–50 nm). The formation of mesoporous structure could be due to the aggregation of $MgIn_2S_4$ and $BiVO_4$. The physical properties of pore structure in different samples were summarized in Table. S1. It can be seen that the values of surface area for different composites increased firstly and then decreased after the addition of $BiVO_4$. Furthermore, the pore volume and pore diameters were determined in the range of 0.027-0.21 m^3/g and 9.10–22.55 nm, respectively.

3.2. Photocatalytic activity

In the case of estimating photocatalytic performance of as-fabricated catalysts, the decompositions of CBZ were executed under visible light illumination (λ > 400 nm). Firstly, we investigated the adsorption ability of different samples. The adsorption percent of CBZ were 3.98, 4.47, 7.70, 9.27, 17.13, 19.84, 20.93, 27.66 and 3.39% for $MgIn_2S_4$, $BS/BiVO_4/MgIn_2S_4$ composites and $BiVO_4$, respectively. As

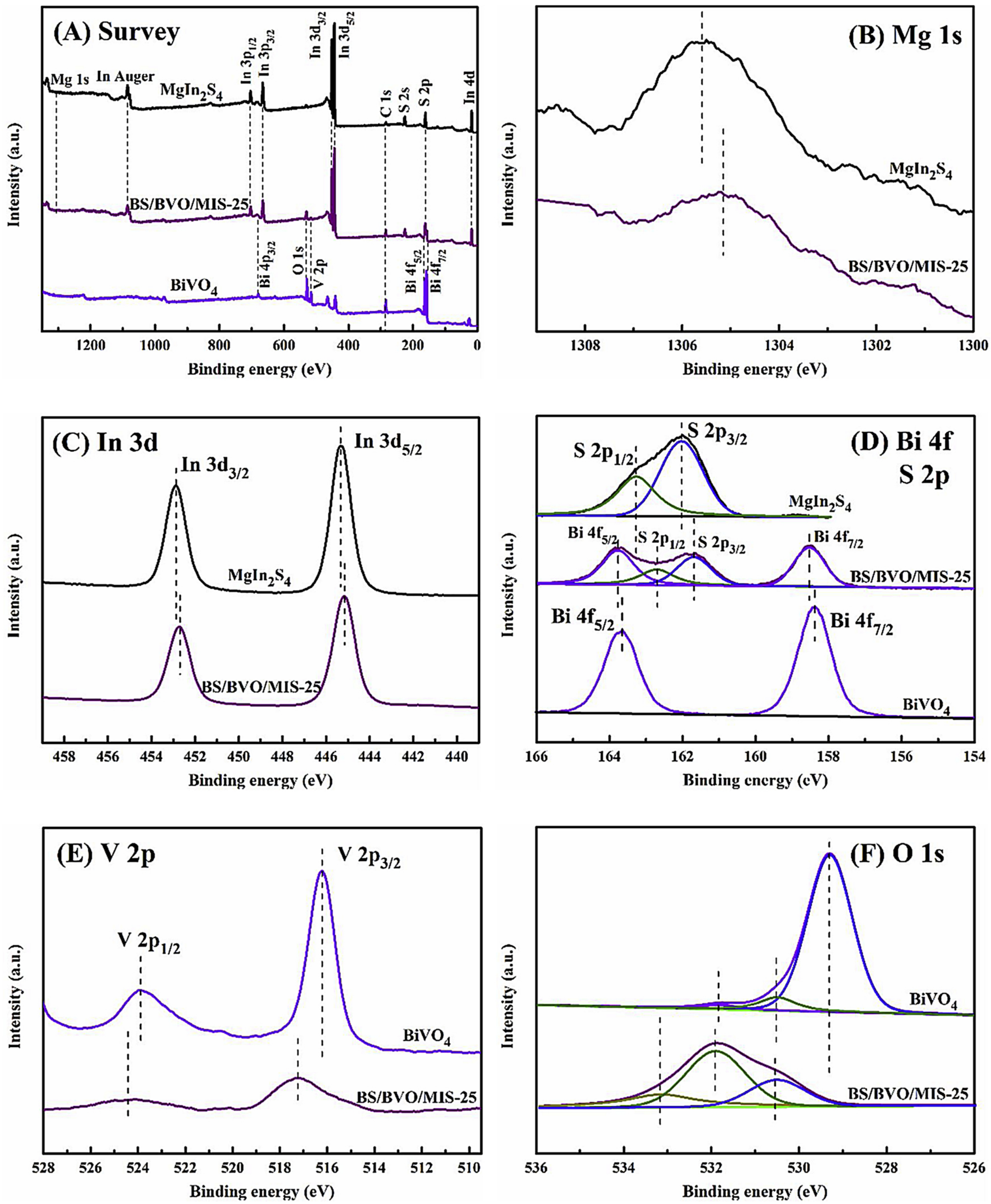

Fig. 3. The XPS spectra of pristine $MgIn_2S_4$, BS/BVO/MIS-25 and pure $BiVO_4$: (A) survey spectra, (B) Mg 1 s, (C) In 3d, (D) Bi 4f and S 2p, (E) V 2p and (F) O 1 s.

can be seen from the degradation results displayed in Fig. 5A, the self-photolysis of CBZ implemented as comparison was insignificant and could be neglected from photocatalytic experiment during this work. For two pure photocatalysts, $MgIn_2S_4$ could be capable of degrading about 15% after 30 min, while $BiVO_4$ exhibited an almost negligible photocatalytic decomposition of CBZ. A considerable enhancement in photocatalytic activity was fulfilled after the assembly of $MgIn_2S_4$ and $BiVO_4$. Concretely, the obtained improvement was higher along with the increasing mass ratio of $BiVO_4$ to $MgIn_2S_4$ from 1% to 25%, and then became lower. Excessive doping of $BiVO_4$ may be response for this phenomena. As we can see from the XRD results, the amount of Bi_2S_3 was progressively increased with the gradually elevating $BiVO_4$ introducing content. The aggregation and overlap of excessive Bi_2S_3 on the surface of $BiVO_4$ may prevent the formation of hetero-junction between Bi_2S_3 and $BiVO_4$. In the meantime, the sunlight was blocked for $BiVO_4$ to be generated photo-induced electrons and holes. All of above factors ultimately lead to the decreased photocatalytic performance when the amount of $BiVO_4$ is larger than 25%. Particularly, the most outstanding degrading efficiency was achieved for BS/BVO/MIS-25 with 99% removal rate of CBZ within 20 min. To be sure, photocatalytic degradation reaction of CBZ in the presence of various catalysts were in keeping with pseudo-first-order kinetics [68]. The apparent rate constants k for the decay of CBZ presented in Fig. 5B were determined to be 0.0049, 0.030, 0.058, 0.11, 0.12, 0.22, 0.091, 0.048 and 0.00052 min^{-1} for $MgIn_2S_4$, BS/BVO/MIS-1, BS/BVO/MIS-2.5, BS/BVO/MIS-5, BS/BVO/MIS-15, BS/BVO/MIS-25, BS/BVO/MIS-40, BS/BVO/MIS-60, and $BiVO_4$, respectively. Startlingly, the k value of BS/BVO/MIS-25 topped the list was about 44.9 and 423.1 times as much as

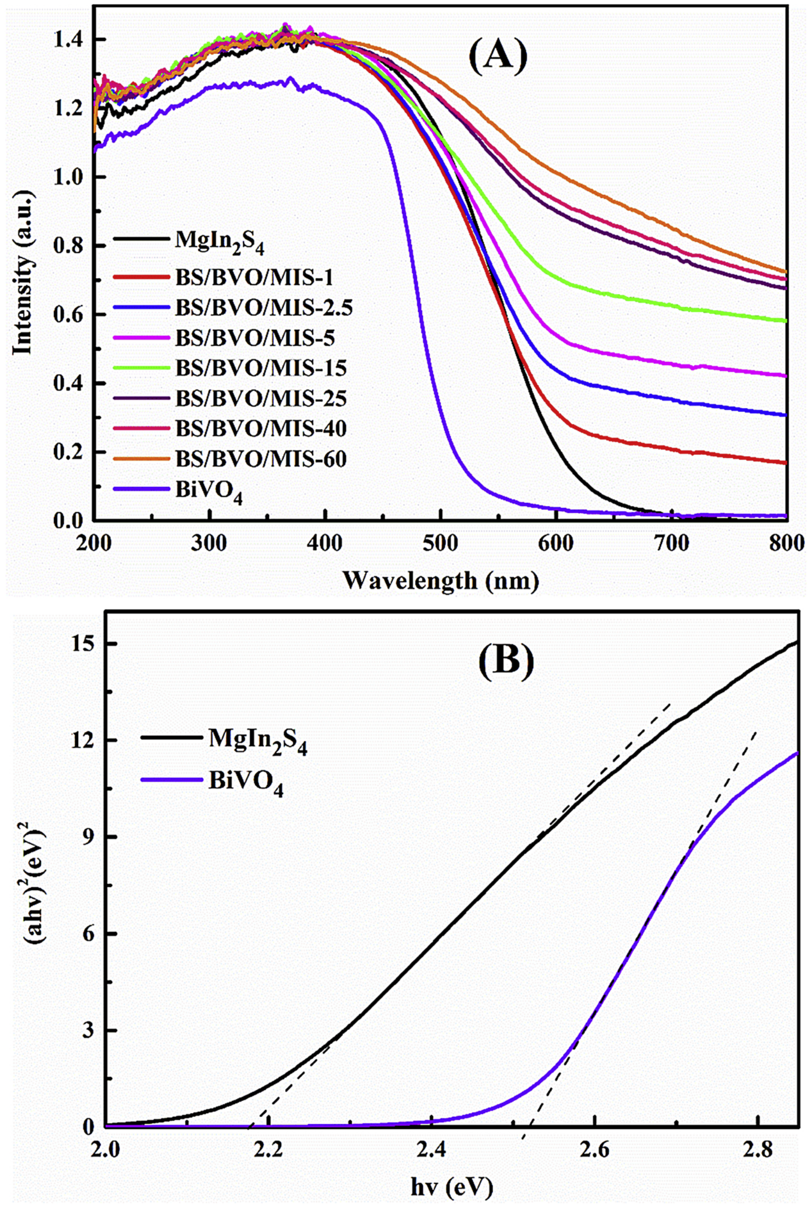

Fig. 4. UV–vis diffuse reflectance spectra of all the samples (A) and plots of $(ah\nu)^2$ versus the photon energy ($h\nu$) for $MgIn_2S_4$ and $BiVO_4$ with the corresponding band gap energies (B).

that of $MgIn_2S_4$ and $BiVO_4$ respectively. Furthermore, the stability of the composites were investigated, and the results were shown in Fig. S2. It can be seen that the degradation percent of CBZ is still higher than 90% after four cycles. The results indicated the good stability of the obtained composite samples.

3.3. Mechanism of the enhanced photocatalytic activities for BS/BVO/MIS composites

According to the results analysis, the superior photocatalytic activity was attained via joint assembly of $MgIn_2S_4$, $BiVO_4$ and Bi_2S_3 by hydrothermal method. To explore the mechanism of enhanced performance for BS/BVO/MIS composites relative to pure $MgIn_2S_4$ and $BiVO_4$, the PL spectra of catalysts were drawn in Fig. 6. Upon the selected excitation wavelength as 379 nm, the peak intensity of $BiVO_4$ was much stronger compared with $MgIn_2S_4$ and BS/BVO/MIS-25. In particular, BS/BVO/MIS-25 exhibited the minimum intensity, revealing the lowest recombination rate of photo-induced electron-hole pairs [69]. The efficient charge separation would be contributed to the conspicuous improvement of photocatalytic performance. The transient photocurrent responses and EIS were also measured to prove the enhanced separation efficiency of the photo-induced electron-hole pairs. It can be seen from Fig. s3 (a) that the composite BS/BVO/MIS-25 exhibited much higher photocurrent than pure $MgIn_2S_4$ and $BiVO_4$. From Fig. s3(b), it can be seen that the BS/BVO/MIS-25 displayed a smaller arc radius than that of $MgIn_2S_4$ and $BiVO_4$. The results indicated that BS/BVO/MIS-25 exhibited superior efficiency of charge transfer and better separation of photoinduced charges.

For purpose of a deeper investigation on mechanism, trapping experiments of oxidative species generated during photocatalytic reactions over BS/BVO/MIS-25, including $^{\cdot}OH$, $^{\cdot}O_2^-$ and h^+, were well enforced. As displayed in Fig. 7, a slight inhibition of degradation rate was observed when ammonium oxalate (AO) was added in reaction system as the quencher of h^+, indicating that h^+ played only a minor supporting role for removal of CBZ. Contrastively, the introduction of Isopropyl alcohol (IPA, the $^{\cdot}OH$ quencher) markedly depressed the decomposition. The vital and irreplaceable role of $^{\cdot}OH$ radical was taken for granted in the photocatalyic reaction of CBZ consequently. In

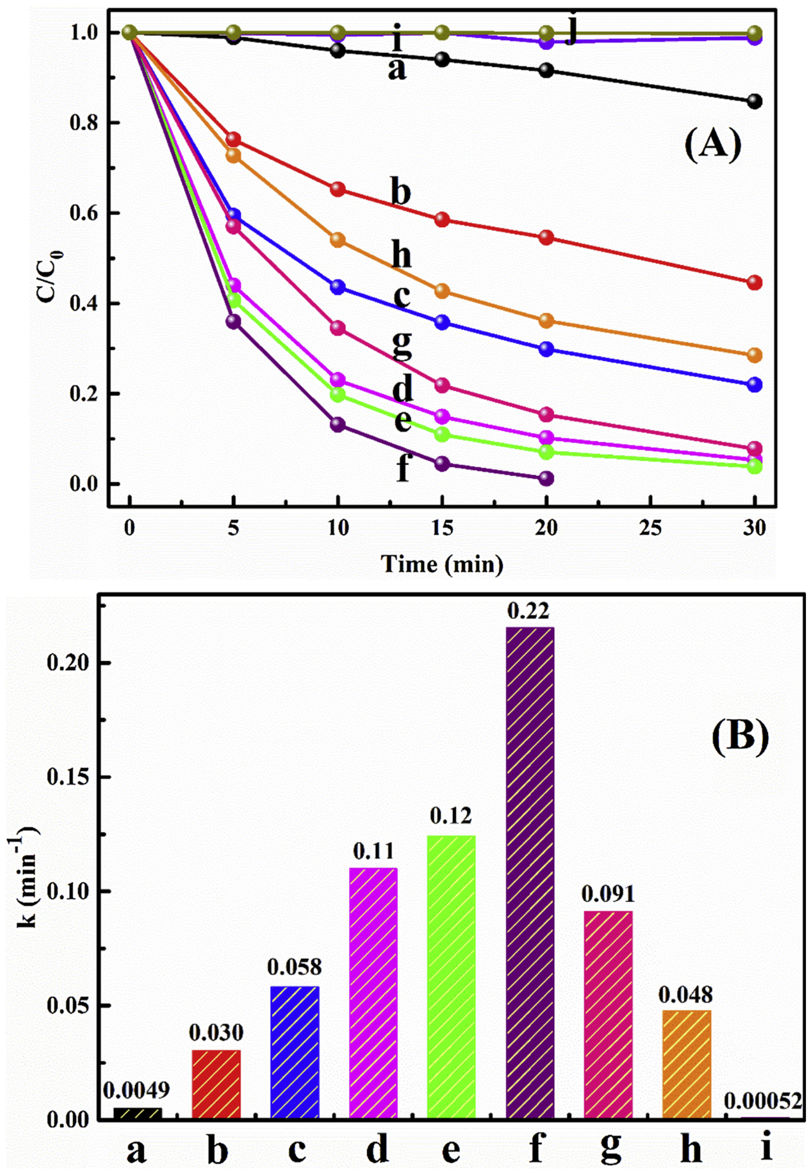

Fig. 5. (A) The photocatalytic decomposition of CBZ over $MgIn_2S_4$ (a), BS/BVO/MIS-x, (x = 1 (b), 2.5 (c), 5 (d), 15 (e), 25 (f), 40 (g) and 60 (h)), $BiVO_4$ (i) and its self-photolysis (j) under visible light illumination, and (B) histogram of the apparent rate constant k for different samples.

addition, the degradation rate was decreased to a certain degree from 99% to 77% with the addition of ascorbic acid (AsA), testifying $^{\cdot}O_2^-$ worked as a secondary active species.

To further identify the active oxidation species over the BS/BVO/MIS-25, the ESR spin-trap techniques were carried out with 5, 5-dimethyl-1-pyrroline-*N*-oxide (DMPO) as scavenger agent, and the results were exhibited in Fig. 8. For whatever DMPO-$^{\cdot}$OH adduct or DMPO-$^{\cdot}O_2^-$ adduct, no obvious signals were observed under the dark condition. Plotted on a graph, the characteristic peaks from both DMPO-$^{\cdot}$OH and DMPO-$^{\cdot}O_2^-$ species were explicitly detected after visible light irradiation for 10 min, which confirmed that $^{\cdot}$OH and $^{\cdot}O_2^-$ could be generated in BS/BVO/MIS-25 system. The intensity of $^{\cdot}$OH was more intense than that of $^{\cdot}O_2^-$, suggesting that $^{\cdot}$OH was the most critical active species while $^{\cdot}O_2^-$ acted as a supplementary role [70], which was in conformity with the results of trapping experiments. Based on the above results, we inferred that the CB electrons could react with oxygen molecules to form $^{\cdot}O_2^-$ radicals and, the VB holes could react with hydroxyl and water molecules to produce $^{\cdot}$OH radicals. Consequently CBZ was oxidized and removed from reaction liquid by $^{\cdot}$OH and $^{\cdot}O_2^-$ with a marginal assistance from h^+.

In order to further explore the generation, migration and reaction processes of photo-excited electrons and holes, the band structures of pure $MgIn_2S_4$ and $BiVO_4$ should be clarified. The valence band edge positions of pure $MgIn_2S_4$ and $BiVO_4$ were ascertained by the XPS valence spectra [71] showed in Fig. 9. The maximum VB edges (E_{VB}) of pristine $MgIn_2S_4$ was presented at about 1.66 eV. While $BiVO_4$ showed a higher value of 2.78 eV, implying a lower top of valence band. Combined with the band gap energies (E_g) of $MgIn_2S_4$ (2.18 eV) and $BiVO_4$ (2.52 eV) from DRS results (Fig. 4B), the minimum CB edges (E_{CB}) were calculated to be -0.52 eV and 0.26 eV, respectively.

Based on the efficient spatial separation of photo-excited charge carriers, two possible mechanisms could be deduced in making clear the enhanced photocatalytic performance in ternary photocatalytic system: conventional hetero-junction pattern and direct Z-scheme pattern which were illustrated in Fig. 10. According to the previous literature reported [45], the band structure of Bi_2S_3 was exhibited in the figure. All $MgIn_2S_4$, $BiVO_4$ and Bi_2S_3 could be optical excited to generate electron-hole pairs under visible light irradiation. As can be seen in Fig. 10, the E_{CB} of $MgIn_2S_4$ (-0.52 V) and Bi_2S_3 were both more negative than that of $BiVO_4$ (0.26 V), while the E_{VB} of $BiVO_4$ (2.78 V) was more

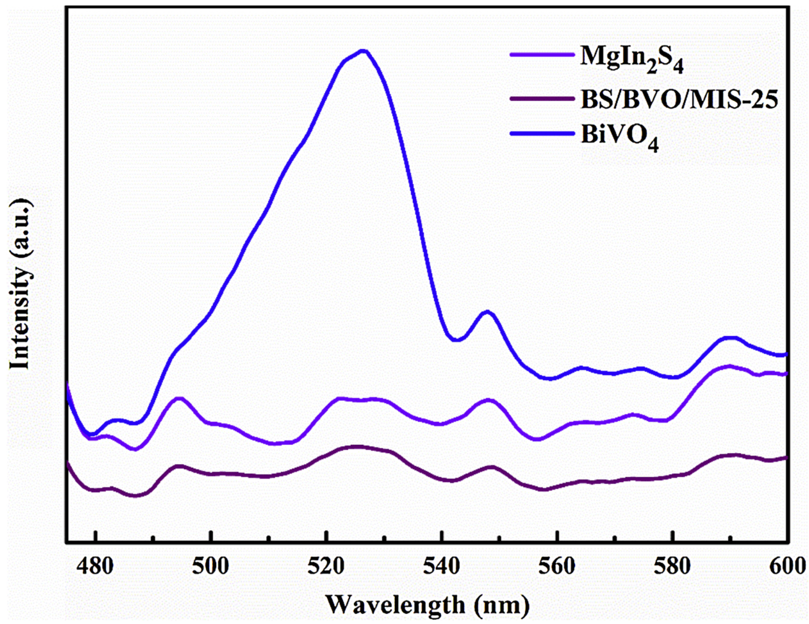

Fig. 6. Photoluminescence spectra of the synthesized $MgIn_2S_4$, BS/BVO/MIS-25 and $BiVO_4$.

positive compared with Bi_2S_3 and $MgIn_2S_4$ (1.66 V) deriving from the XPS valence spectra. In conventional hetero-junction pattern, photo-induced electrons in conduction band were transferred from $MgIn_2S_4$ and Bi_2S_3 to $BiVO_4$, whereas photo-generated holes in valence band possessed opposite migration direction. It is noteworthy that the redox abilities of conduction band electrons on $BiVO_4$ and valence band holes on $MgIn_2S_4$ and Bi_2S_3 were weaker than the potential of $O_2/^{\cdot}O_2^-$ (-0.33 eV) and $^{\cdot}OH/H_2O$ (+ 2.68 eV) as well as $^{\cdot}OH/OH^-$ (+ 1.99 eV), respectively. In this case, $^{\cdot}O_2^-$ and $^{\cdot}OH$ radicals could not be generated, which opposite with the results of trapping experiments and ESR spin-trap measurements. Furthermore, the electron migration direction was inconsistent with XPS analysis in which electrons transfer from the surface of $BiVO_4$ to that of $MgIn_2S_4$ on the $Bi_2S_3/BiVO_4/MgIn_2S_4$ composites. As for the direct Z-scheme pattern, the excited electrons in the CB of $BiVO_4$ were transferred and combined with photo-induced holes in the VB of $MgIn_2S_4$ and Bi_2S_3 through $BiVO_4$-$MgIn_2S_4$ and $BiVO_4$-Bi_2S_3 interfaces respectively upon the visible light illumination due to the migration rate of electrons were faster than that of holes. Hence, the electrons in CB of $MgIn_2S_4$ and Bi_2S_3, holes in VB of $BiVO_4$ could be separated effectively, which was beneficial to photocatalytic decomposition of CBZ. And the migration result was completely in conformity with XPS analysis. Note that the CB potential of $MgIn_2S_4$ and Bi_2S_3 were capable of reducing dissolved oxygen molecules to $^{\cdot}O_2$-radicals, while adsorbed water, and OH group could be oxidized to $^{\cdot}OH$ radicals by the VB potential of $BiVO_4$. Subsequently, generated active oxygen species ($^{\cdot}OH$ and $^{\cdot}O_2^-$) could oxidize and remove CBZ in water corresponding to trapping experiments and ESR spin-trap results. To our delight, a dual-*Z*-scheme type for transfer paths of photo-excited electrons and holes was formed in $Bi_2S_3/BiVO_4/MgIn_2S_4$ composites. As a result, direct dual-*Z*-scheme pattern was the most possible mechanism actually rather than conventional hetero-junction pattern to explain the improved photocatalytic activity in degrading CBZ.

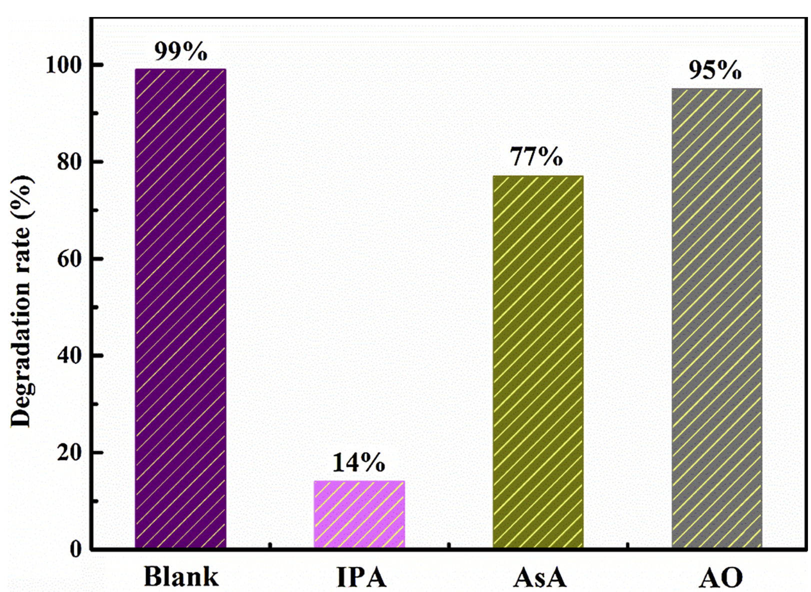

Fig. 7. Photocatalytic degradation rate of CBZ by BS/BVO/MIS-25 with the addition of different scavengers under visible light irradiation.

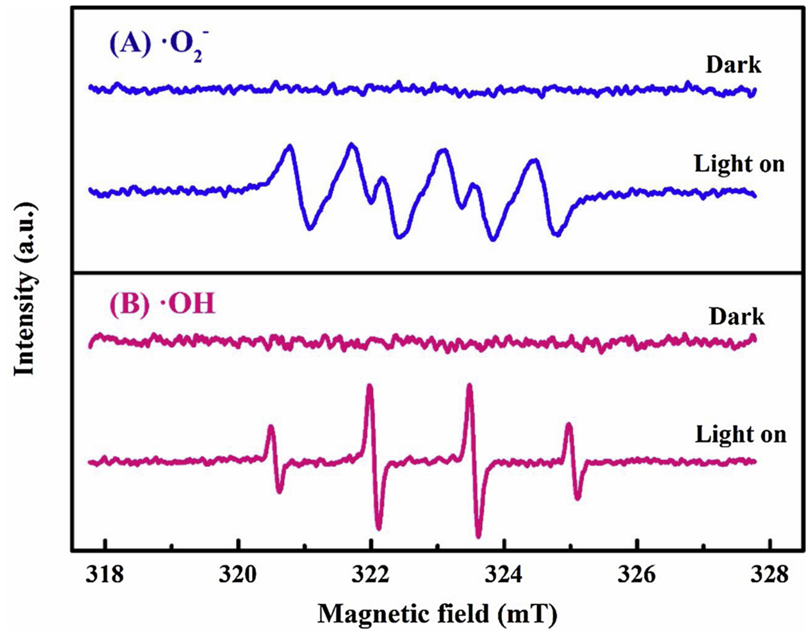

Fig. 8. DMPO spin-trapping ESR spectra of (A) DMPO-$^\cdot O_2^-$ and (B) DMPO-$^\cdot$OH for BS/BVO/MIS-25 under dark and visible light irradiation (λ > 400 nm) for 10 min.

With reference to the above-mentioned analysis results, the following reasons could be employed to account for the improved photocatalytic degradation activities of $Bi_2S_3/BiVO_4/MgIn_2S_4$ composites: 1) the light absorption of $Bi_2S_3/BiVO_4/MgIn_2S_4$ composites was expanded in visible wavelength region because of the existence of Bi_2S_3; 2) the adsorption rates of $Bi_2S_3/BiVO_4/MgIn_2S_4$ composites were increased with elevated $BiVO_4$ levels; 3) the formation of direct dual-*Z*-scheme hetero-junctions between $BiVO_4$ and $MgIn_2S_4$ as well as $BiVO_4$ and Bi_2S_3 facilitated the charge separation; 4) electrons in CB of $MgIn_2S_4$ and Bi_2S_3, holes in VB of $BiVO_4$ participated in degradation reaction were on different semiconductors with non-interference; 5) the stronger reducibility of electrons and stronger oxidizability of holes were retained for photocatalytic degradation reaction.

3.4. Proposed reaction pathways of CBZ by BS/BVO/MIS-25

On the basis of degradation by-products analyzed qualitatively by LC-ESI-MS/MS chromatography and the pertinent literatures, the hypothetical reaction pathways of CBZ (m/z = 237 g/mol) by BS/BVO/MIS-25 under visible light irradiation were proposed in Fig. 11. In terms of ESR results (Fig. 8) and trapping experiment (Fig. 7), $^\cdot$OH and $^\cdot O_2^-$ radicals were generated and principally involved in the decomposition of CBZ in the presence of BS/BVO/MIS-25, which lead to a main pathway for $^\cdot$OH and $^\cdot O_2^-$ induced degradation. It is generally known that hydroxylation is prone to occur at the olefinic bond with higher frontier electron density (FED) [72]. As a result, P1 (di-hydroxy CBZ, m/z = 271) could be generated and further hydroxylated to form P2 (tri-hydroxy CBZ, m/z = 287) from a C-centered radical cation under

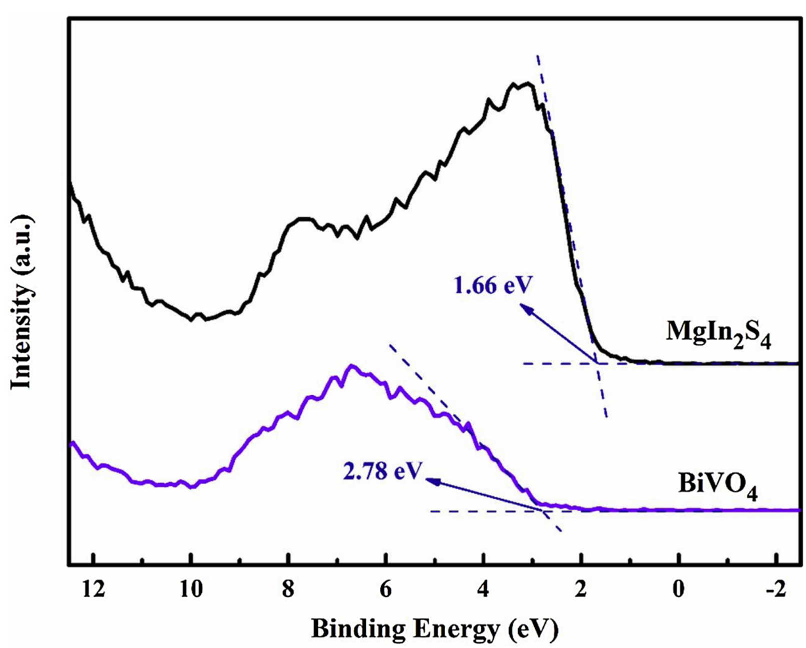

Fig. 9. Valence-band XPS spectra of the pure $MgIn_2S_4$ and $BiVO_4$ samples.

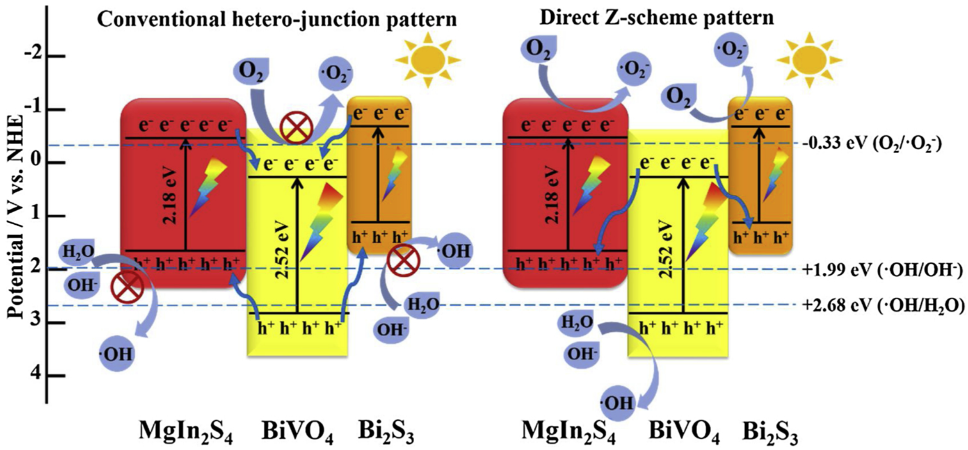

Fig. 10. The charge transfer mechanism for $Bi_2S_3/BiVO_4/MgIn_2S_4$ composites under visible light irradiation.

the progressively attacks of ˙OH [73,74]. An alternative pathway would be the formation of P3 (m/z = 253 g/mol) resulted from the electrophilic attack of the $^{\cdot}O_2{}^{-}$ or ˙OH on olefinic double bond of the central heterocyclic ring [75]. As for by-product P3, it could undergo a cleavage reaction of epoxy bond in azepine ring to produce P4 (m/z = 267 g/mol) [2]. Followed by a further aldehyde oxidation, P5 (m/z = 301 g/mol) and P6 (m/z = 285 g/mol) were produced consequently. On the other hand, P7 (m/z = 208 g/mol) was generated after hydrogen rearrangement reaction and the loss of the amides groups (−CONH2) of P3 [68]. Subsequently, P7 may be converted into P8 (m/z = 180 g/mol) via oxidation reaction, which followed by the generation of P9 (m/z = 195 g/mol) as the further oxidation product [76]. Additionally, P10 (m/z = 224 g/mol) was detected as hydroxyl adducts of P7 [77,78]. It was warrantable supposition that all of the

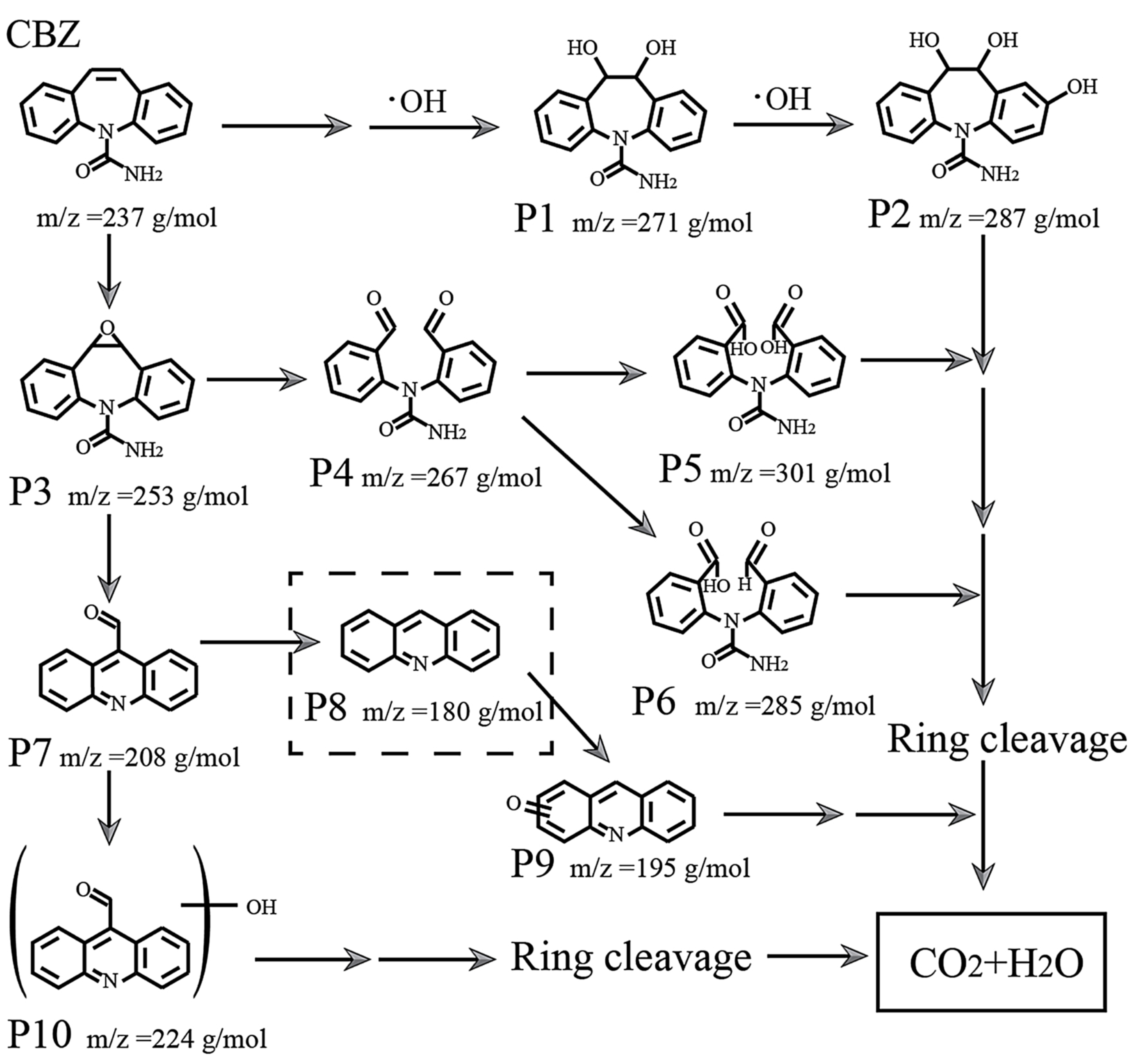

Fig. 11. Proposed degradation pathways of CBZ in the presence of BS/BVO/MIS-25 under visible light illumination.

intermediate products could eventually be mineralized into CO_2 and H_2O after undergoing further oxidation and ring-cleavage reaction by $^{\cdot}OH$, h^+ and $^{\cdot}O_2^-$ [79–82].

4. Conclusions

To summary, we have successful fabricated a series of direct Z-scheme $Bi_2S_3/BiVO_4/MgIn_2S_4$ hybrid photocatalysts via hydrothermal method. According to characterization results, $MgIn_2S_4$ were generated on the surface of $BiVO_4$ with intimate interfacial contact, and Bi_2S_3 were formed and attached to $BiVO_4$. $Bi_2S_3/BiVO_4/MgIn_2S_4$ nanocomposits exhibit superior photocatalytic activities in contrast to pristine $MgIn_2S_4$ and pure $BiVO_4$ in degrading CBZ under UV light irradiation. Note that the highest photocatalytic performance for CBZ removal is observed on BS/BVO/MIS-25 with the optimal proportion of $BiVO_4$, which was about 44.9 and 423.1 times as much as that of $MgIn_2S_4$ and $BiVO_4$. A direct Z-scheme migration mechanism is proved to be responsible for the enhanced photocatalytic performance of $Bi_2S_3/BiVO_4/MgIn_2S_4$ composites rather than the conventional heterojunction-type mechanism. CBZ was oxidized and removed from reaction liquid by $^{\cdot}OH$ and $^{\cdot}O_2^-$ with a marginal assistance from h^+. The intermediates were identified and an inferred degradation pathway of CBZ over BS/BVO/MIS-25 was proposed on the basis of HPLC-ESI-MS/MS results. We hope that this work can offer a few new deep insights into design and synthesis of $MgIn_2S_4$-based direct Z-scheme-type compositions for photocatalytic technology and environment restoration.

Acknowledgements

We are grateful for grants from National Science Funds for Creative Research Groups of China (No.51421006), Natural Science Foundation of China (51679063), the Fundamental Research Funds for The Central Universities (2018B14514), the Key Program of National Natural Science Foundation of China (No. 91647206), the National Key Plan for Research and Development of China (2016YFC0502203), Fundamental Research Funds (No. 2016B43814), and PAPD.

Appendix A. Supplementary data

Supplementary material related to this article can be found, in the online version, at doi:https://doi.org/10.1016/j.apcatb.2019.04.031.

References

[1] H. Gulyas, M.K. Ogun, W. Meyer, M. Reich, R. Otterpohl, Inadequacy of carbamazepine-spiked model wastewaters for testing photocatalysis efficiency, Sci. Total Environ. 542 (2016) 612–619.
[2] L.L. Bo, K.B. He, N. Tan, B. Gao, Q.Q. Feng, J.D. Liu, L. Wang, Photocatalytic oxidation of trace carbamazepine in aqueous solution by visible-light-driven Znln(2)S (4): performance and mechanism, J. Environ. Manage. 190 (2017) 259–265.
[3] Y.B. Ding, G.L. Zhang, X.R. Wang, L.H. Zhu, H.Q. Tang, Chemical and photocatalytic oxidative degradation of carbamazepine by using metastable Bi^{3+} self-doped $NaBiO_3$ nanosheets as a bifunctional material, Appl. Catal. B 202 (2017) 528–538.
[4] Y.Z. He, C.M. Dai, X.F. Zhou, Magnetic cobalt ferrite composite as an efficient catalyst for photocatalytic oxidation of carbamazepine, Environ. Sci. Pollut. Res. Int. 24 (2) (2017) 2065–2074.
[5] Y.B. Ding, H.B. Tang, S.H. Zhang, S.B. Wang, H.Q. Tang, Efficient degradation of carbamazepine by easily recyclable microscaled $CuFeO_2$ mediated heterogeneous activation of peroxymonosulfate, J. Hazard. Mater. 317 (2016) 686–694.
[6] F. Chen, Q. Yang, Y.L. Wang, J.W. Zhao, D.B. Wang, X.M. Li, Z. Guo, H. Wang, Y.C. Deng, C.G. Niu, G.M. Zeng, Novel ternary heterojunction photcocatalyst of Ag nanoparticles and $g\text{-}C_3N_4$ nanosheets co-modified $BiVO_4$ for wider spectrum visible-light photocatalytic degradation of refractory pollutant, Appl. Catal. B Environ. 205 (2017) 133–147.
[7] M. Tobajas, C. Belver, J.J. Rodriguez, Degradation of emerging pollutants in water under solar irradiation using novel TiO_2-ZnO/clay nanoarchitectures, Chem. Eng. J. 309 (2017) 596–606.
[8] H. Yamashita, K. Mori, Y. Kuwahara, T. Kamegawa, M.C. Wen, P. Werma, M. Che, Single-site and nano-confined photocatalysts designed in porous materials for environmental uses and solar fuels, Chem. Soc. Rev. 47 (2018) 8072–8096.
[9] S. Ramasundaram, M.G. Seid, W. Lee, C. Ul Kim, E.-J. Kim, S.W. Hong, K.J. Choi, Preparation, characterization, and application of TiO_2-patterned polyimide film as a photocatalyst for oxidation of organic contaminants, J. Hazard. Mater. 340 (2017) 300–308.
[10] D.D. Tang, G.K. Zhang, Ultrasonic-assistant fabrication of cocoon-like $Ag/AgFeO_2$ nanocatalyst with excellent plasmon enhanced visible-light photocatalytic activity, Ultrason. Sonochem. 37 (2017) 208–215.
[11] K. Iwashina, A. Iwase, S. Nozawa, S.-i Adachi, A. Kudo, Visible-light-responsive $CuLi_{1/3}Ti_{2/3}O_2$ powders prepared by a molten CuCI treatment of Li_2TiO_3 for photocatalytic H-2 evolution and Z-schematic water splitting, Chem. Mater. 28 (13) (2016) 4677–4685.
[12] Y. Kanigaridou, A. Petala, Z. Frontistis, M. Antonopoulou, M. Solakidou, I. Konstantinou, Y. Deligiannakis, D. Mantzavinos, D.I. Kondarides, Solar photocatalytic degradation of bisphenol A with $CuO_x/BiVO_4$: insights into the unexpectedly favorable effect of bicarbonates, Chem. Eng. J. 318 (2017) 39–49.
[13] R.P. Antony, T. Baikie, S.Y. Chiam, Y. Ren, R.R. Prabhakar, S.K. Batabyal, S.C.J. Loo, J. Barber, L.H. Wong, Catalytic effect of Bi^{5+} in enhanced solar water splitting of tetragonal $BiV_{0.8}Mo_{0.2}O_4$, Appl. Catal. A Gen. 526 (2016) 21–27.
[14] J.J. Yang, D.M. Chen, Y. Zhu, Y.M. Zhang, YF Zhu, 3D-3D porous Bi_2WO_6/graphene hydrogel composite with excellent synergistic effect of adsorption-enrichment and photocatalytic degradation, Appl. Catal. B Environ. 205 (2017) 228–237.
[15] W.H. Dong, D.D. Wu, J.M. Luo, Q.J. Xing, H. Liu, J.P. Zou, X.B. Luo, X.B. Min, H.L. Liu, S.L. Luo, C.T. Au, Coupling of photodegradation of RhB with photoreduction of CO_2 over rGO/$SrTi_{0.95}Fe_{0.05}O_3$-delta catalyst: a strategy for one-pot conversion of organic pollutants to methanol and ethanol, J. Catal. 349 (2017) 218–225.
[16] D. Yue, D.M. Chen, Z.H. Wang, H. Ding, R.L. Zong, Y.F. Zhu, Enhancement of visible photocatalytic performances of a Bi_2MoO_6-BiOCl nanocomposite with plate-on-plate heterojunction structure, J. Chem. Soc. Faraday Trans. 16 (47) (2014) 26314–26321.
[17] Y.N. Huo, M. Miao, Y. Zhang, J.A. Zhu, H.X. Li, Aerosol-spraying preparation of a mesoporous hollow spherical $BiFeO_3$ visible photocatalyst with enhanced activity and durability, Chem. Commun. 47 (7) (2011) 2089–2091.
[18] D.S. Cook, Y. Wu, K. Lienau, R. More, R.J. Kashtiban, O.V. Magdysyuk, G.R. Patzke, R.I. Walton, Time-resolved powder X-ray diffraction of the solvothermal crystallization of cobalt gallate spinel photocatalyst reveals transient layered double hydroxides, Chem. Mater. 29 (12) (2017) 5053–5057.
[19] A. Akhundi, A. Habibi-Yangjeh, Graphitic carbon nitride nanosheets decorated with $CuCr_2O_4$ nanoparticles: novel photocatalysts with high performances in visible light degradation of water pollutants, J. Colloid Interface Sci. 504 (2017) 697–710.
[20] L.F. Shen, Q. Che, H.S. Li, X.G. Zhang, Mesoporous $NiCo_2O_4$ nanowire arrays grown on carbon textiles as binder-free flexible electrodes for energy storage, Adv. Funct. Mater. 24 (18) (2014) 2630–2637.
[21] H. Liu, J. Zhang, D. Ao, Construction of heterostructured $ZnIn_2S_4$@NH_2-MIL-125(Ti) nanocomposites for visible-light-driven H-2 production, Appl. Catal. B-Environ. 221 (2018) 433–442.
[22] T. Wang, Y.Y. Chai, D.K. Ma, W. Chen, W.W. Zheng, S.M. Huang, Multidimensional CdS nanowire/$CdIn_2S_4$ nanosheet heterostructure for photocatalytic and photoelectrochemical applications, Nano Res. 10 (8) (2017) 2699–2711.
[23] J.J. Ding, X.Y. Li, L. Chen, X. Zhang, S. Sun, J. Bao, C. Gao, X.Y. Tian, Au-Pt alloy nanoparticles site-selectively deposited on $CaIn_2S_4$ nanosteps as efficient photocatalysts for hydrogen production, J. Mater. Chem. A 4 (32) (2016) 12630–12637.
[24] D.L. Jiang, J. Li, C.S. Xing, Z.Y. Zhang, S.C. Meng, M. Chen, Two-dimensional Caln (2)S(4)/$g\text{-}C_3N_4$ heterojunction nanocomposite with enhanced visible-light photocatalytic activities: interfacial engineering and mechanism insight, ACS Appl. Mater. Interfaces 7 (34) (2015) 19234–19242.
[25] Y.H. Lin, F. Zhang, D.C. Pan, H.X. Li, Y.F. Lu, Sunlight-driven photodegradation of organic pollutants catalyzed by TiO_2/(ZnS)(x)(CuInS2)(1-x) nanocomposites, J. Mater. Chem. 22 (18) (2012) 8759–8763.
[26] C. Xue, H. An, X.Q. Yan, J.L. Li, B.L. Yang, J.J. Wei, G.D. Yang, Spatial charge separation and transfer in ultrathin $CdIn_2S_4$/rGO nanosheet arrays decorated by ZnS quantum dots for efficient visible-light-driven hydrogen evolution, Nano Energy 39 (2017) 513–523.
[27] X. Chen, L. Li, W.Z. Zhang, Y.X. Li, Q. Song, L. Dong, Fabricate globular flower- like $CuS/CdIn_2S_4/ZnIn_2S_4$ with high visible light response via microwave-assisted one-step method and its multipathway photoelectron migration properties for hydrogen evolution and pollutant degradation, ACS Sustain. Chem. Eng. 4 (12) (2016) 6680–6688.
[28] H. Liu, Z. Zhang, J.C. Meng, J. Zhang, Novel visible-light-driven $CdIn_2S_4$/mesoporous $g\text{-}C_3N_4$ hybrids for efficient photocatalytic reduction of CO2 to methanol, Mol. Catal. 430 (2017) 9–19.
[29] G. Yang, D.M. Chen, H. Ding, J.J. Feng, J.Z. Zhang, Y.F. Zhu, S. Hamid, D.W. Bahnemann, Well-designed 3D $ZnIn_2S_4$ nanosheets/TiO_2 nanobelts as direct Z-scheme photocatalysts for CO_2 photoreduction into renewable hydrocarbon fuel with high efficiency, Appl. Catal. B Environ. 219 (2017) 611–618.
[30] W.J. Wang, G.Y. Li, D.H. Xia, T.C. An, H.J. Zhao, P.K. Wang, Photocatalytic nanomaterials for solar-driven bacterial inactivation: recent progress and challenges, Environ. Sci. Nano 4 (2017) 782–799.
[31] W.J. Wang, T.W. Ng, W.K. Ho, J.H. Huang, S.J. Liang, T.C. An, G.Y. Li, J.C. Yu, P.K. Wong, CdIn2S4 microsphere as an efficient visible-light-driven photocatalyst for bacterial inactivation: Synthesis, characterizations and photocatalytic inactivation mechanisms, Appl. Catal. B 129 (2013) 482–490.
[32] R. Lucena, J.C. Conesa, I. Aguilera, P. Palacios, P. Wahnon, V-substituted In_2S_3: an intermediate band material with photocatalytic activity in the whole visible light range, J. Mater. Chem. A 2 (22) (2014) 8236–8245.
[33] D. Santamaria-Perez, M. Amboage, F.J. Manjon, D. Errandonea, A. Munoz, P. Rodriguez-Hernandez, A. Mujica, S. Radescu, V.V. Ursaki, I.M. Tiginyanu, Crystal

chemistry of $CdIn_2S_4$, $MgIn_2S_4$, and $MnIn_2S_4$ thiospinels under high pressure, J. Phys. Chem. C 116 (26) (2012) 14078–14087.
[34] W. Chen, Y.X. Hua, Y. Wang, T. Huang, T.Y. Liu, X.H. Liu, Two-dimensional mesoporous g-C_3N_4 nanosheet-supported $MgIn_2S_4$ nanoplates as visible-light-active heterostructures for enhanced photocatalytic activity, J. Catal. 349 (2017) 8–18.
[35] L. Tian, X. Yang, X. Cui, Q. Liu, H. Tang, Fabrication of dual direct Z-scheme g-C_3N_4/MoS_2/Ag_3PO_4 photocatalyst and its oxygen evolution performance, Appl. Surf. Sci. 463 (2019) 9–17.
[36] W.J. Wang, T.C. An, G.Y. Li, D.H. Xia, H.J. Zhao, J.C. Yu, P.K. Wang, Earth-abundant Ni_2P/g-C_3N_4 lamellar nanohydrids for enhanced photocatalytic hydrogen evolution and bacterial inactivation under visible light irradiation, Appl. Catal. B 217 (2017) 570–580.
[37] D.H. Xia, W.J. Wang, R. Yin, Z.F. Jiang, T.C. An, G.Y. Li, H.J. Zhao, P.K. Wong, Enhanced photocatalytic inactivation of Escherichia coli by a novel Z-scheme g-C_3N_4/m-Bi_2O_4hybrid photocatalyst under visible light: the role of reactive oxygen species, Appl. Catal. B 214 (2017) 23–33.
[38] Q.Z. Wang, J.J. He, Y.B. Shi, S.L. Zhang, T.J. Niu, H.D. She, Y.P. Bi, Z.Q. Lei, Synthesis of MFe_2O_4 (M = Ni, Co)/$BiVO_4$ film for photolectrochemical hydrogen production activity, Appl. Catal. B Environ. 214 (2017) 158–167.
[39] W.J. Wang, Y. Yu, T.C. An, G.Y. Li, H.Y. Yip, J.C. Yu, P.K. Wong, Visible-light-Driven photocatalytic inactivation of E. Coli K-12 by bismuth vanadate nanotubes: bactericidal performance and mechanism, Environ. Sci. Technol. 46 (2012) 4599–4606.
[40] L.J. Song, Y.Y. Pang, Y.J. Zheng, C.F. Chen, L. Ge, Design, preparation and enhanced photocatalytic activity of porous BiOCl/$BiVO_4$ microspheres via a coprecipitation-hydrothermal method, J. Alloys Compd. 710 (2017) 375–382.
[41] L.L. Zhang, W.H. Feng, B. Wang, K.Q. Wang, F. Gao, Y. Zhao, P. Liu, Construction of dual-channel for optimizing Z-scheme photocatalytic system, Appl. Catal. B-Environ. 212 (2017) 80–88.
[42] Y.C. Deng, L. Tang, G.M. Zeng, C.Y. Feng, H.R. Dong, J.J. Wang, H.P. Feng, Y.N. Liu, Y.Y. Zhou, Y. Pang, Plasmonic resonance excited dual Z-scheme $BiVO_4$/Ag/Cu_2O nanocomposite: synthesis and mechanism for enhanced photocatalytic performance in recalcitrant antibiotic degradation, Environ. Sci. Nano 4 (7) (2017) 1494–1511.
[43] X.Q. Wu, J. Zhao, L.P. Wang, M.M. Han, M.L. Zhang, H.B. Wang, H. Huang, Y. Liu, Z.H. Kang, Carbon dots as solid-state electron mediator for $BiVO_4$/CDs/CdS Z -scheme photocatalyst working under visible light, Appl. Catal. B Environ. 206 (2017) 501–509.
[44] Y.J. Yuan, D.Q. Chen, S.H. Yang, L.X. Yang, J.J. Wang, D.P. Cao, W.G. Tu, Z.T. Yu, Z.G. Zou, Constructing noble-metal-free Z-scheme photocatalytic overall water splitting systems using MoS_2 nanosheet modified CdS as a H-2 evolution photocatalyst, J. Mater. Chem. A 5 (40) (2017) 21205–21213.
[45] A. Iwase, S. Yoshino, T. Takayama, Y.H. Ng, R. Amal, A. Kudo, Water splitting and CO_2 reduction under visible light irradiation using Z-scheme Systems consisting of metal sulfides, CoO_x-loaded $BiVO_4$, and a reduced graphene oxide electron mediator, J. Am. Chem. Soc. 138 (32) (2016) 10260–10264.
[46] D.L. Guan, C.G. Niu, X.J. Wen, H. Guo, C.H. Deng, G.M. Zeng, Enhanced Escherichia coli inactivation and oxytetracycline hydrochloride degradation by a Z-scheme silver iodide decorated bismuth vanadate nanocomposite under visible light irradiation, J. Colloid Interface Sci. 512 (2017) 272–281.
[47] M. Zhao, Y.H. Fu, H.C. Ma, C. Ma, X.L. Dong, X.F. Zhang, Synthesis, characterization and photoreactivity of hierarchically N-doped $(BiO)_2CO_3$/Bi_2S_3 with highly exposed {001} facets, Mater. Des. 93 (2016) 1–8.
[48] Y. Liu, Y.D. Shi, X. Liu, H.X. Li, A facile solvothermal approach of novel Bi_2S_3/TiO_2/RGO composites with excellent visible light degradation activity for methylene blue, Appl. Surf. Sci. 396 (2017) 58–66.
[49] A. Chen, Z.Y. Bian, J. Xu, X. Xin, H. Wang, Simultaneous removal of Cr(VI) and phenol contaminants using Z-scheme bismuth oxyiodide/reduced graphene oxide/bismuth sulfide system under visible-light irradiation, Chemosphere 188 (2017) 659–666.
[50] X.H. Gao, H.B. Wu, L.X. Zheng, Y.J. Zhong, Y. Hu, X.W. Lou, Formation of mesoporous heterostructured $BiVO_4$/Bi_2S_3 hollow discoids with enhanced photoactivity, Angew. Chem. Int. Ed. 53 (23) (2014) 5917–5921.
[51] W.Y. Wang, X.W. Wang, C.X. Zhou, B. Du, J.X. Cai, G. Feng, R.B. Zhang, Bi_2S_3-nanowire-sensitized $BiVO_4$ sheets for enhanced visible-light photoelectrochemical activities, J. Phys. Chem. C 121 (35) (2017) 19104–19111.
[52] D.K. Ma, M.L. Guan, S.S. Liu, Y.Q. Zhang, C.W. Zhang, Y.X. He, S.M. Huang, Controlled synthesis of olive-shaped Bi_2S_3/$BiVO_4$ microspheres through a limited chemical conversion route and enhanced visible-light-responding photocatalytic activity, J. Chem. Soc. Dalton Trans. 41 (18) (2012) 5581–5586.
[53] J.Z. Wang, J. Jin, X.G. Wang, S.N. Yang, Y.L. Zhao, Y.W. Wu, S.Y. Dong, J.Y. Sun, J.H. Sun, Facile fabrication of novel $BiVO_4$/Bi_2S_3/MoS_2 n-p heterojunction with enhanced photocatalytic activities towards pollutant degradation under natural sunlight, J. Colloid Interface Sci. 505 (2017) 805–815.
[54] F.Q. Zhou, J.C. Fan, Q.J. Xu, Y.L. Min, $BiVO_4$ nanowires decorated with CdS nanoparticles as Z-scheme photocatalyst with enhanced H-2 generation, Appl. Catal. B-Environ. 201 (2017) 77–83.
[55] N. Liang, J.T. Zai, M. Xu, Q. Zhu, X. Wei, X.F. Qian, Novel Bi_2S_3/$Bi_2O_2CO_3$ heterojunction photocatalysts with enhanced visible light responsive activity and wastewater treatment, J. Mater. Chem. A 2 (12) (2014) 4208–4216.
[56] Y.H. Ao, L.Y. Xu, P.F. Wang, C. Wang, J. Hou, J. Qian, Preparation of CdS nanoparticle loaded flower-like $Bi_2O_2CO_3$ heterojunction photocatalysts with enhanced visible light photocatalytic activity, Dalton Trans. 44 (25) (2015) 11321–11330.
[57] R. Chen, P.F. Wang, J. Chen, C. Wang, Y.H. Ao, Synergetic effect of MoS2 and MXene on the enhanced H_2 evolution performance of CdS under visible light irradiation, Appl. Surf. Sci. 473 (2019) 11–19.
[58] H.G. Yu, P. Xiao, P. Wang, J.G. Yu, Amorphous molybdenum sulfide as highly efficient electron-cocatalyst for enhanced photocatalytic H_2 evolution, Appl. Catal. B-Environ. 193 (2016) 217–225.
[59] T. Liu, G.Q. Tan, C.C. Zhao, C. Xu, Y.N. Su, Y. Wang, H.J. Ren, A. Xia, D. Shao, S.M. Yan, Enhanced photocatalytic mechanism of the Nd-Er co-doped tetragonal $BiVO_4$ photocatalysts, Appl. Catal. B-Environ. 213 (2017) 87–96.
[60] L. Wang, G.R. Yang, S.J. Peng, J.N. Wang, D.X. Ji, W. Yan, S. Ramakrishna, Fabrication of $MgTiO_3$ nanofibers by electrospinning and their photocatalytic water splitting activity, Int. J. Hydrogen Energy 42 (41) (2017) 25882–25890.
[61] W. Chen, T. Huang, Y.X. Hua, T.Y. Liu, X.H. Liu, S.M. Chen, Hierarchical $CdIn_2S_4$ microspheres wrapped by mesoporous g-C_3N_4 ultrathin nanosheets with enhanced visible light driven photocatalytic reduction activity, J. Hazard. Mater. 320 (2016) 529–538.
[62] H.G. Yu, C. Cao, X.F. Wang, J.G. Yu, Ag-modified BiOCl single-crystal nanosheets: dependence of photocatalytic performance on the region-selective deposition of Ag nanoparticles, J. Phys. Chem. C 121 (2017) 13191–13201.
[63] J.P. Zou, J. Ma, J.M. Luo, J. Yu, J.K. He, Y.T. Meng, Z. Luo, S.K. Bao, H.L. Liu, S.L. Luo, X.B. Luo, T.C. Chen, S.L. Suib, Fabrication of novel heterostructured few layered WS_2-Bi_2WO_6/$Bi_{3.84}W_{0.16}O_{6.24}$ composites with enhanced photocatalytic performance, Appl. Catal. B-Environ. 179 (2015) 220–228.
[64] S. Song, H. Yang, C.L. Zhou, J. Cheng, Z.B. Jiang, Z. Lu, J. Miao, Underwater superoleophobic mesh based on $BiVO_4$ nanoparticles with sunlight-driven self-cleaning property for oil/water separation, Chem. Eng. J. 320 (2017) 342–351.
[65] X. Lin, D. Xu, Y. Xi, R. Zhao, L.N. Zhao, M.S. Song, H.J. Zhai, G.B. Che, L.M. Chang, Construction of leaf-like g-C_3N_4/Ag/$BiVO_4$ nanoheterostructures with enhanced photocatalysis performance under visible-light irradiation, Colloids Surf. A Physicochem. Eng. Asp. 513 (2017) 117–124.
[66] W.L. Yu, D.F. Xu, T.Y. Peng, Enhanced photocatalytic activity of g-C_3N_4 for selective CO_2 reduction to CH_3OH via facile coupling of ZnO: a direct Z-scheme mechanism, J. Mater. Chem. A 3 (39) (2015) 19936–19947.
[67] S. Singh, R. Sharma, B.R. Mehta, Enhanced surface area, high Zn interstitial defects and band gap reduction in N-doped ZnO nanosheets coupled with $BiVO_4$ leads to improved photocatalytic performance, Appl. Surf. Sci. 411 (2017) 321–330.
[68] W.K. Jo, T.S. Natarajan, Influence of TiO_2 morphology on the photocatalytic efficiency of direct Z-scheme g-C_3N_4/TiO_2 photocatalysts for isoniazid degradation, Chem. Eng. J. 281 (2015) 549–565.
[69] Y.F. Li, R.X. Jin, X. Fang, Y. Yang, M. Yang, X.C. Liu, Y. Xing, S.Y. Song, In situ loading of Ag_2WO_4 on ultrathin g-C_3N_4 nanosheets with highly enhanced photocatalytic performance, J. Hazard. Mater. 313 (2016) 219–228.
[70] P.M. Sirimanne, N. Sonoyama, T. Sakata, Semiconductor sensitization by microcrystals of $MgIn_2S_4$ on wide bandgap $MgIn_2O_4$, J. Solid State Chem. 154 (2) (2000) 476–482.
[71] T.Y. Xu, R.L. Zhu, G.Q. Zhu, J.X. Zhu, X.L. Liang, Y.P. Zhu, H.P. He, Mechanisms for the enhanced photo-Fenton activity of ferrihydrite modified with $BiVO_4$ at neutral pH, Appl. Catal. B-Environ. 212 (2017) 50–58.
[72] Y. Guo, P.F. Wang, J. Qian, Y.H. Ao, C. Wang, J. Hou, Phosphate group grafted twinned $BiPO_4$ with significantly enhanced photocatalytic activity: synergistic effect of improved charge separation efficiency and redox ability, Appl. Catal. B 234 (2018) 90–99.
[73] X. Yang, L. Tian, X. Zhao, H. Tang, Q. Liu, G. Li, Interfacial optimization of g-C3N4-based Z-scheme heterojunction toward synergistic enhancement of solar-driven photocatalytic oxygen evolution, Appl. Catal. B-Environ. 244 (2019) 240–249.
[74] J. Di, J.X. Xia, M.X. Ji, H.P. Li, H. Xu, H.M. Li, R. Chen, The synergistic role of carbon quantum dots for the improved photocatalytic performance of Bi_2MoO_6, Nanoscale 7 (26) (2015) 11433–11443.
[75] Z. Wan, G.K. Zhang, X.Y. Wu, S. Yin, Novel visible-light-driven Z-scheme $Bi_{12}GeO_{20}$/g-C_3N_4photocatalyst: Oxygen-induced pathway of organic pollutants degradation and proton assisted electron transfer mechanism of Cr(VI) reduction, Appl. Catal. B-Environ. 207 (2017) 17–26.
[76] X.Y. Gao, X.C. Zhang, Y.W. Wang, S.Q. Peng, B. Yue, C.M. Fan, Photocatalytic degradation of carbamazepine using hierarchical BiOCl microspheres: Some key operating parameters, degradation intermediates and reaction pathway, Chem. Eng. J. 273 (2015) 156–165.
[77] Y.F. Rao, W. Chu, Y.R. Wang, Photocatalytic oxidation of carbamazepine in triclinic-WO_3 suspension: role of alcohol and sulfate radicals in the degradation pathway, Appl. Catal. A Gen. 468 (2013) 240–249.
[78] R. Meribout, Y. Zuo, A.A. Khodja, A. Piram, S. Lebarillier, J.S. Cheng, C. Wang, P. Wong-Wah-Chung, Photocatalytic degradation of antiepileptic drug carbamazepine with bismuth oxychlorides (BiOCl and BiOCl/AgCl composite) in water: Efficiency evaluation and elucidation degradation pathways, J. Photochem. Photobiol. A Chem. 328 (2016) 105–113.
[79] H.C. Chen, X.N. Wang, W.L. Bi, Y.L. Wu, W.B. Dong, Photodegradation of carbamazepine with BiOCl/Fe_3O_4 catalyst under simulated solar light irradiation, J. Colloid Interface Sci. 502 (2017) 89–99.
[80] T.F. Xu, D.J. Ni, X. Chen, F. Wu, P.F. Ge, W.Y. Lu, H.G. Hu, Z.X. Zhu, W.X. Chen, Self-floating graphitic carbon nitride/zinc phthalocyanine nanofibers for photocatalytic degradation of contaminants, J. Hazard. Mater. 317 (2016) 17–26.
[81] C. Martinez, L. M Canle, M.I. Fernandez, J.A. Santaballa, J. Faria, Kinetics and mechanism of aqueous degradation of carbamazepine by heterogeneous photocatalysis using nanocrystalline TiO_2, ZnO and multi-walled carbon nanotubes-anatase composites, Appl. Catal. B-Environ. 102 (3-4) (2011) 563–571.
[82] A. Jelic, I. Michael, A. Achilleos, E. Hapeshi, D. Lambropoulou, S. Perez, M. Petrovic, D. Fatta-Kassinos, D. Barcelo, Transformation products and reaction pathways of carbamazepine during photocatalytic and sonophotocatalytic treatment, J. Hazard. Mater. 263 (2013) 177–186.